A Parameterization for the Triggering of Landscape-Generated Moist Convection. Part I: Analysis of High-Resolution Model Results

BARRY H. LYNN*

Columbia University Center for Climate Systems Research, New York, New York

WEI-KUO TAO

Mesoscale Atmospheric Processes Branch, NASA Goddard Space Flight Center, Greenbelt, Maryland

FRANK ABRAMOPOULOS

Science Systems and Applications Inc., NASA Goddard Institute for Space Studies, New York, New York

(Manuscript received 4 January 1999, in final form 5 July 2000)

ABSTRACT

To develop a parameterization for the triggering of moist convection by landscape-generated mesoscale circulations, a set of relatively high-resolution three-dimensional (3D) simulations was produced. These simulations modeled the development of landscape generated mesoscale circulations that triggered moist convection over west-to-east dry patches. No clear relationship existed between average patch size and average rainfall. Rather, rainfall averaged over the area of individual patches varied linearly with the size of these patches. Thus, cumulus parameterization schemes need to account for a population of clouds (over individual patches) within each domain of a large-scale atmospheric model (i.e., numerical weather prediction and global circulation models).

It is demonstrated that mesoscale perturbations in velocity, temperature, and moisture need to be included in triggering functions when evaluating whether moist convection will occur. Yet, the largest patches did not always produce the largest mesoscale perturbations. Instead, the size of the perturbations depended upon the ratio of the local radius of deformation to patch size, the gradient of soil moisture between patches, as well as large-scale environmental conditions such as wind, stability, and specific humidity. These perturbations can be used to improve the representation of triggering functions associated with moist convection over landscape patches. Appropriate dimensionless numbers that can be used in a parameterization for the mesoscale perturbations are identified.

1. Introduction

Analysis of observational data and simulation results obtained over heterogeneous land surfaces can reveal both turbulent and mesoscale processes. For example, turbulent eddies can be superimposed upon mesoscale circulations that are generated by landscape discontinuities (Mahrt 1987; Balling 1988; Segal et al. 1989; Smith et al. 1992; Mahrt et al. 1994; Chen and Avissar 1994; Wang et al. 1996; Pielke et al. 1997; Vidale et al. 1997; Avissar and Schmidt 1998; Lynn et al. 1998). These mesoscale circulations form when the atmosphere over relatively dry ground (or nontranspiring vegetation) is heated more than the atmosphere over wet ground (or transpiring vegetation). They generate sea-breeze-like fronts, which can be associated with relatively large vertical velocity, temperature, and moisture perturbations. Studies with numerical models and some observational results have shown that these sea-breeze-like fronts produce both shallow and deep convection (e.g., Chen and Avissar 1994; Cutrim et al. 1995; Hong et al. 1995; Avissar and Liu 1996; Lynn et al. 1998).

In the past, parameterizations of atmospheric moist processes in large-scale atmospheric models have been developed by dividing cumulus clouds into two groups, nonprecipitating and precipitating (Frank 1983). The former are shallow clouds that have a vertical depth of about 3 km, while precipitating clouds extend vertically into the middle- and upper-troposphere, and often form in very unstable atmospheres (Zawadzki et al. 1981; Frank 1983). Parameterizations of shallow clouds usu-

* Current affiliation: Department of Atmospheric Sciences, The Hebrew University of Jerusalem, Jerusalem, Israel.

Corresponding author address: Dr. Barry Lynn, Department of Atmospheric Sciences, The Hebrew University of Jerusalem, Jerusalem, 91904, Israel.
E-mail: barry@dina.es.huji.ac.il

ally assume that these clouds are triggered by Rayleigh-Bénard convective instability [i.e., turbulent-scale processes (Wetzel and Boone 1995)]. Parameterizations of deep clouds, for the most part, relate the triggering of these clouds to large-scale forcings, for example, the magnitude of the grid-scale moisture convergence [for a summary, see Kain and Fritsch (1992)].

Rogers and Fritsch (1996) discuss a relatively new type of triggering function that includes the impact of landscape-generated mesoscale circulations (LGMCs) on the triggering variables. They estimate the mesoscale contribution to the total perturbation in vertical velocity as follows:

$$w_i = k_1 \frac{\Delta X}{L}\left(1 - \frac{h_{sl}}{H}\right). \quad (1)$$

Here, k_1 is a coefficient of proportionality that varies in space as a function of surface properties, ΔX is the grid size, L is the grid-length scale beneath that cloud-scale perturbations begin to be resolved explicitly ($\approx$5 km), h_{sl} is the midheight of the source layer above the ground in meters, and H is the threshold height above which surface-based and lower-tropospheric perturbations are assumed to become negligible. Hong and Pan (1998) propose a similar formulation for the mesoscale contribution to subgrid-scale temperature.

However, Rogers and Fritsch (1996) [and Hong and Pan (1998)] lacked an appropriate dataset by which to formulate the relationship expressed by Eq. (1). Thus, they assume that the coefficient k_1 is a constant, and ignore the effect of background wind and atmospheric stability. Moreover, w_i increases with patch size, which they include indirectly through the relationship between w_i and the size of the grid element of the hosting model. Since, the likelihood that their ''trigger'' will activate moist convection increases with the size of the perturbation, the effect of their formulation is that domains with larger average patch size should produce the most rainfall.

Here, we use a high-resolution three-dimensional cloud-resolving model to simulate the atmospheric response to heating of west-to-east landscape patches (described in section 2). The complete (modeled) output (used as our dataset) consists of simulation results from model domains with patch sizes of different lengths and initial atmospheric conditions. The purpose is (i) to show the relationship between patch size and rainfall, (ii) to demonstrate the importance of the mesoscale contribution to the triggering of moist convection, and (iii) to determine the relationship between the mesoscale perturbations (including specific humidity) and patch size, surface properties such as soil moisture, as well as stability and background wind. These are discussed in section 3. We further suggest dimensionless numbers to be used in a parameterization. A summary and conclusion is presented in section 4. In Part II (Lynn and Tao 2001), we present a zero-order and first-order parameterization for the triggering of moist convection over landscape patches.

TABLE 1. Model input parameters used for numerical simulations. Numbers in parentheses refer to simulations with moist processes ''turned on.''

Condition	Value
Day of the year	July 27
Latitude	28°
Initialization time	6 A.M.
Integration time step	5 s
Simulation length	15 (12) h
Height of the atmosphere	10 km (20 km)
Number of vertical grid elements	30 (50)
Vertical grid resolution (stretched)	20–500 m
Lateral boundary conditions	Periodic
Horizontal grid resolution (fixed)	250 m × 250 m

2. Method

a. Numerical model

A dataset derived from observations that could be used for a study of the type presented here does not exist. Such a study requires very high-resolution data over a relatively large area (>1000 km^2). Fortunately, recent improvements in computer power have made possible a large number of high-resolution model simulations. Some of these simulations have been applied to the study of convective processes over heterogeneous land surfaces (Nichols et al. 1991; Chen and Avissar 1994; Doran and Zhong 1995; Fankauser et al. 1995; Avissar and Liu 1996; Lynn et al. 1998). Still, we note that observations like those with aircraft (e.g., Young 1987, 1988; Finkele et al. 1995; Mahrt et al. 1994; Sellers et al. 1995) and Doppler radar (Houze 1989) can provide the data required to verify model derived results and parameterizations.

We used the Goddard Cumulus Ensemble Model (GCE; Tao and Simpson 1993) to obtain high-resolution model output. Briefly, the Rutledge and Hobbs (1984) microphysics scheme was used here to parameterize precipitation processes. The GCE model uses a prognostic equation for the turbulent kinetic energy based on work by Deardorff (1975), Klemp and Wilhelmson (1978), and Soong and Ogura (1980); and the model includes Parameterization for Land–Atmosphere Convective Exchange (PLACE), described by Wetzel and Boone (1995). Note, this version of the PLACE model does not include anything but the soil and land model components of the original PLACE model.

b. Experimental domain and model experiments

The experimental domain had a 250 m × 250 m horizontal grid resolution with periodic lateral boundary conditions, and a stretched vertical coordinate (see Table 1 for more details). Each simulation was run for 15 h with a time step of 5 s. The total domain size was 512

TABLE 2. Land characteristics used for the numerical simulations.

Land characteristic	Value
Surface roughness (m)	1.11
Surface albedo	0.20
Surface emissivity	1.00
Soil texture	Sandy-clay-loam
Soil depth (m)	10
Root zone depth (m)	1.60
Porosity ($mm^3\ mm^{-3}$)	0.404
Field capacity ($mm^3\ mm^{-3}$)	0.298
Wilting point ($mm^3\ mm^{-3}$)	0.137
Slope of retention curve	6.77
Saturated matric potential (cm)	−13.49
Saturated hydraulic conductivity ($cm\ s^{-1}$)	4.45×10^{-4}
Vegetation	Tall, broadleaf, and needleleaf trees
Leaf area index	2.46
Minimum stomatal resistance ($s\ m^{-1}$)	1.00
Maximum stomatal resistance ($s\ m^{-1}$)	10.0
Plant critical water potential (m)	−200

grid elements in the west-to-east (x) direction (or 128 km) and 32 grid elements in the north-to-south (y) direction (8 km).

Ideally, this study would have used a domain whose size varied the same in the x and y direction. Available computer capability, unfortunately, did not allow us to simulate such a domain. Thus, the mesoscale circulations are generated by essentially two-dimensional patches. Yet, the domain was wide enough to simulate three-dimensional turbulence, and the horizontal west-to-east structure of mesoscale circulations that developed were very similar to those obtained in three-dimensional simulations over patches (e.g., Lynn et al. 1995b).

Two soundings on 27 July 1991, one located on the east coast and one located on the west coast of Florida, were taken from the Convection and Electrification Experiment (CaPE). They were averaged to obtain a mean sounding for an east–west cross section over the peninsula at 0600 LST (Fig. 1). The sounding had a small initial convective available potential energy (CAPE)[1] of 740 kJ kg^{-1}, but a relatively low lifting condensation level (LCL) pressure (an LCL of 1010 mb with a surface pressure of 1018 mb), low level of free convection (LFC) (LFC of 839 mb), and high equilibrium level (EL) (EL of 190 mb). The vertical profile of the u component of the wind is shown in Fig. 1b (the v component was set equal to zero simply because we would expect it to have no important effect on the developing mesoscale circulations in the ''truncated'' north-to-south domain used here). The speed of the u wind in the lower troposphere is small enough to allow for the development of landscape-generated mesoscale circulations, but large enough to affect this development (see below). Upon moistening of the planetary boundary layer (PBL), the initial sounding was conducive to the development of deep moist convection.

We initialized the numerical model with a uniformly distributed homogeneous vegetation consisting of a broad-leaf and coniferous forest. The stomatal resistance of the vegetation is a strong function of soil moisture in the root zone. For this reason, the soil moisture of sandy-clay-loam was chosen to ''control'' the surface distribution of land surface fluxes, leading to the generation of mesoscale circulations in our simulated domains (see Table 2 for more details). The process by which landscape circulations are generated by contrasting patches of wet and dry ground has been described in detail by Pielke et al. (1991), Avissar and Chen (1993), and Lynn et al. (1995b). We will not discuss this further and the reader is referred to these papers for further details.

Various land surface domains were used here to provide the surface boundary conditions; they are listed in Table 3. In most, there were (different) alternating distributions of patches of dry and wet ground. In the dry ground, the volumetric soil moisture was chosen to be 10% of the fraction of the difference between field capacity and wilting point.[2] Here, this corresponds to a soil moisture, $\theta_{sl} = 0.153$. In the wet ground, this fraction was set at 90% of field capacity ($\theta_{sl} = 0.282$). Superimposed on each grid element was a random value of volumetric soil wetness, r, which was $-0.02 \leq r \leq 0.02$. Land surface patches with $\theta_{sl} = 0.153$ are referred to as ''dry patches,'' while land surface patches with $\theta_{sl} = 0.282$ are referred to as ''wet patches.''

[1] The CAPE was calculated using a mixed layer depth from the land surface to 500 m.

[2] Wilting point is the moisture content corresponding to matric potential of −15 bar, it is close to the volumetric water content at which plants can no longer extract water from the soil. The field capacity is the volumetric water content corresponding to a balance that occurs in wet soil between diffusion (up) and gravitational drainage (down).

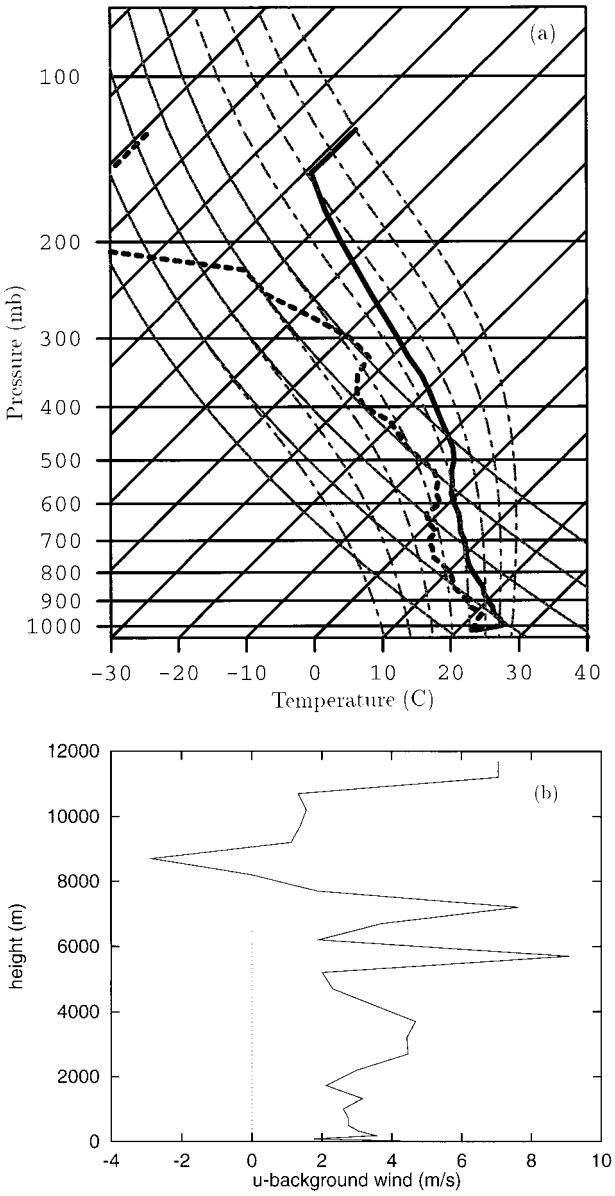

FIG. 1. Atmospheric sounding obtained from CaPE. (a) Skew T diagram of temperature and dewpoint; (b) profile of the initial, u component of the background wind.

Four of the 10 domains are shown in Fig. 2, and are labeled domains 1–4. In the main body of the text, we discuss in detail only results from domains 1 and 3, while we refer briefly to domains 2 and 4 for the purposes of scale separation. In domain 1, there is a 64-km dry patch surrounded by two 32-km wet patches. Because the domain is periodic, there is actually a 64-km dry patch and 64-km wet patch in this domain. Note, the patches within the domains vary only in the west-to-east direction. In comparison, there were a number of differently sized dry patches in domain 3. They are (left to right) 7.5, 4, 16, 4, 8, 20, and 4 km in length. Domain 2 contains patches

TABLE 3. Description of land surface domains.

Name	Patch sizes (L, km)
Domain 1	64
Domain 2	16, 24, 24.5
Domain 3	7.5, 4, 16, 4, 8, 20, 4
Domain 4	$0.25 < L < 1$
Domain 5	40, 32
Domain 6	$3 < L < 8$
Domain 7	$2 < L < 6$
Domain 8	64, $\theta_{sl} = 0.177$ (dry patches), $\theta_{sl} = 0.257$ (wet patches)
Domain 9	64, Sinusoidal distribution, $\theta_{sl_{min}} = 0.177$, $\theta_{sl_{max}} = 0.257$
Domain 10	64, Jagged distribution for soil moisture

of intermediate size, while domain 4 contains very small patches. Domains 5–7, also listed in Table 3, have patches of either intermediate or very small size.

The 8th, 9th, and 10th domains were used to test the senstivity of the model results to soil moisture gradients. In domain 8, the wet and dry patches of domain 1 had smaller moisture contrast than domain 1 (see Table 3). In domain 9, the soil moisture varied as a sinusoidal wave across the domain, with maxima at the domain edges and a minima at the center of the domain. We used this domain to examine the sensitivity of the triggering variables to the sharpness of the moisture gradient. In domain 10, the soil moisture first resembled domain 1 (wth 64-km patches), but then was modified in the regions adjoining the inner halves of each wet and dry patch. These regions became patches with average size of about 3 km. Here, one can argue that this is a domain with a 64-km dry patch, but with jagged edges; or, one can argue that this is a 32-km dry patch surrounded by 48-km wet patches with jagged edges. Recognizing that the constrast in soil moisture can be irregular, we used domain 10 to examine the sensivity of the triggering variables to such a distribution.

All domains are idealized representations of those that occur in situ. Still, the range of idealized domains chosen provides useful simulation results from which to draw conclusions about the potential impact of in situ landscape discontinuities on moist convection. In fact, the simulated impact of the landscape on the organized mesoscale flow was similar to that of Wang et al. (1998), who used a statistical parameterization of the land surface heterogeneity. Avissar and Schmidt (1998) note that sharp gradients in heat fluxes exist in many locations, including, among others, agricultural areas in arid regions, deforested areas next to unperturbed forests, and along coast lines of lakes and oceans.

A summary of all simulations produced in this study can be found in Table 4. Eleven simulations were produced using the domains described in Table 4a, with moist processes ''turned on'' (experiments 1w–11w). These simulations tested the relationship between patch size, background wind, and rainfall. Twenty simulations were produced with moist processes ''turned off'' (Table 4b). By

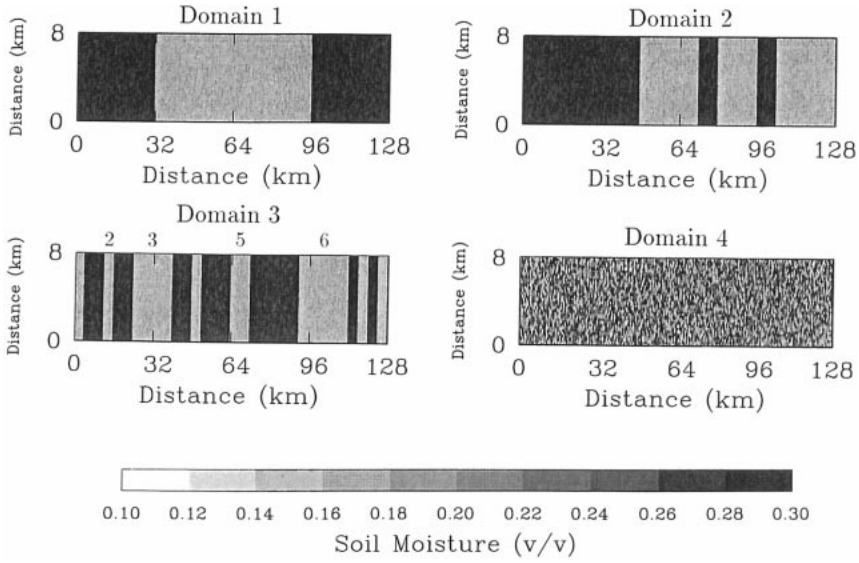

FIG. 2. Distribution of land surface domains in some of the numerical experiments.

turned off, we mean that no clouds were allowed to form in the simulated domain, and the atmosphere was allowed to supersaturate. These simulations allowed us to easily identify the triggering variables as well as test their relationship to patch size, soil moisture gradients, wind, stability, and latitude. Note, the difference between experiments with and without moist processes will be compared.

The reader should keep in mind that saturation is determined by the mean, resolved variables, and the size of the perturbations from the mean: and that the moisture profile can vary independently of air temperature. Furthermore, in Part II we develop a parameterization for the perturbations from the mean, which are our set of triggering variables. Moreover, the parameterization for the triggering variables is sensitive to changes in the forcing of LGMCs by moist convection. This is important because we later show that moist convection can affect the vertical structure and magnitude of the triggering variables.

c. Scale analysis and triggering variables

To obtain a possible set of triggering variables, we examined modeled atmospheric fields at various times during the model simulations. These atmospheric fields were the modeled perturbation fields of horizontal wind (u_s), vertical velocity (w_s), potential temperature (θ_s), and specific humidity (q_s). The analysis indicated, like that of Rogers and Fritsch (1996), that the most robust parcels occur in parcels along sea-breeze-like fronts, and that one could consider vertical velocity, temperature, or moisture in a triggering function, or various combinations of these variables. Here, these variables of the triggering function are referred to as w_o, θ_o, and q_o.

To obtain parcels, one can take the average of the modeled fields over a square area of arbitrary size (square areas were chosen here, rather than circular areas, out of convenience). To determine a potential triggering parcel's $w_o(z)$, $\theta_o(z)$, and $q_o(z)$, we first found the location of the largest mesoscale (see below) vertical velocity perturbation. This was on each sea-breeze-like front moving inward from each side of a dry patch. Then, we found along this front the largest total vertical velocity. The location of the largest vertical velocity along the front became the center of the parcel.

The profiles of the triggering variables can be decomposed into mesoscale (single prime), large eddy-turbulent or cloud-scale (double prime), and small eddy-turbulent or (triple prime) components. Then,

$$\phi_o = \phi_o' + \phi_o'' + \phi_o'''. \tag{2}$$

To use the high-resolution model output to obtain the components of ϕ_o, note that any model variable ϕ can be separated into a resolved and subresolvable component:

$$\phi = \tilde{\phi} + \phi_s, \tag{3}$$

where the $\tilde{\phi}$ represents the large-scale (i.e., the grid size in regional- or global-scale models), and ϕ_s is the perturbation superimposed on it. The flow component, ϕ_s, includes all motions on scales smaller than the large-scale or synoptic flow; that is,

$$\phi_s = \phi' + \phi'' + \phi'''. \tag{4}$$

Observations suggest that small, turbulent eddies have horizontal length scales of about 50 m, while turbulent large eddies have horizontal length sale of about 1–1.5 times the boundary layer height (H; Hardy and Ottersten 1969; Konrad 1970; Kaimal et al. 1976; Caughey and Palmer 1979; Taconet and Weill 1983). The timescale of these turbulent circulations is less than an hour. In comparison, mesoscale circulations have spatial scale of about 10–200 km, and timescale 50 min–1 day (e.g., Stull 1988; Vidale et al. 1997). Note, the decomposition

TABLE 4a. Description of model experiments with moist processes turned on. The v component of the wind was set equal to 0.

Name	Patch sizes (L, km)	Special condition
Exp. 1w	64 (domain 1)	Background u wind a constant, 0.5 m s^{-1}
Exp. 2w	40, 32	Background u wind a constant, 0.5 m s^{-1}
Exp. 3w	16, 24, 24.5 (domain 2)	Background u wind a constant, 0.5 m s^{-1}
Exp. 4w	7.5, 4, 16, 4, 8, 20, 4 (domain 3)	Background u wind a constant, 0.5 m s^{-1}
Exp. 5w	$3 < L < 8$	Background u wind a constant, 0.5 m s^{-1}
Exp. 6w	$2 < L < 6$	Background u wind a constant, 0.5 m s^{-1}
Exp. 7w	$0.25 < L < 1$ (domain 4)	Background u wind a constant, 0.5 m s^{-1}
Exp. 8w	64	Observed u background wind
Exp. 9w	16, 24, 24.5	Observed u background wind
Exp. 10w	40, 32	Observed u background wind
Exp. 11w	7.5, 4, 16, 4, 8, 20, 4	Observed u background wind

of ϕ_s is independent of the grid scale of the cloud-resolving model, although cloud models can provide the dataset (model output) for this decomposition.

We also assume that

$$\phi = \tilde{\phi} + \phi' + \phi'' + \phi''' \quad \text{and} \tag{5}$$

$$\langle\phi\rangle = \langle\tilde{\phi} + \phi' + \phi'' + \phi'''\rangle = \tilde{\phi}, \tag{6}$$

where the angle brackets $\langle\ \rangle$ indicate an average of the variable ϕ (and its components) at the grid scale of a regional- or global-scale atmospheric model.

If the flow is one-dimensional, the variables, $\tilde{\phi}$, ϕ', ϕ'', and ϕ''' can be formally defined from a discrete Fourier transform (e.g., Walker 1988) as

$$\phi_j = \frac{1}{N}\sum_{j=0}^{N-1} \Phi_k e^{i2\pi jk/N} \tag{7}$$

such that

$$\tilde{\phi} = \frac{1}{N}\Phi_o, \tag{8}$$

$$\phi' = \frac{1}{N}\sum_{j=1}^{N_{\phi'-1}} \Phi_k e^{i2\pi jk/N}, \tag{9}$$

$$\phi'' = \frac{1}{N}\sum_{j=N_{\phi'}}^{N_{\phi''-1}} \Phi_k e^{i2\pi jk/N}, \tag{10}$$

$$\phi''' = \frac{1}{N}\sum_{j=N_{\phi''}}^{N-1} \Phi_k e^{i2\pi jk/N}. \tag{11}$$

Here, $N_{\phi'-1}$ has a value that results in a filtering of both the large and small turbulent eddies from the modeled output [i.e., the wavenumber whose range should be chosen between $H/\Delta x$ to $1.5H/\Delta x$ (where Δx is the grid spacing in the numerical model)]. The field remaining after filtering[3] is $\tilde{\phi} + \phi'$, from which ϕ' can be simply calculated. Likewise, the large eddies are found through the specification of an appropriate value for $N_{\phi''-1}$ (i.e., 50 m/Δx). In this case, the fields remaining would be $\tilde{\phi} + \phi' + \phi''$. Given both $\tilde{\phi}$ and ϕ', ϕ'' can also be calculated.

We calculated the boundary layer height across the domain and used the maximum boundary layer height to obtain $N_{\phi'-1}$. We then examined the vertical profiles of triggering variables (with size 5.1 km; typical of cloud bases), obtained after assuming that turbulent eddies have wavelength from 1.5 to 3.5 (in increments of 0.5) times the boundary layer height (H). The distribution of the atmospheric fields were most sensitive to filtering in the range of values $1.5H$–$2.5H$. However, the distribution of the filtered fields did not change very much when we used a wavelength of $3.0H$ or $3.5H$. This implies that when we used, for example, a wavelength of 3.0 times the boundary layer height, that this value enabled a filtering of the large eddies from the modeled output, leaving the mesoscale fields.

To show that we could filter out the large and small eddies, we did a spectral analysis of the horizontal wind (Fig. 3) obtained in simulations using the domains shown in Fig. 2. This analysis revealed that the dominant spectral energy (in the u wind field) corresponds to the wavenumber of the surface forcing. For example, peaks in the power spectrum occurred, for example. for wavenumber 4 (e.g., patch #3 in domain 3; a 32-km dry–wet patch couplet) and wavenumber 7 (patch #5 in domain 3; an 18-km couplet). Most importantly, a simulation of very small patches ($\approx$0.25 km^2; domain 4), produced an energy spectrum with wavelengths smaller than about 10 km. The energy associated with wavelengths greater than 10 km was mesoscale-kinetic energy (Avissar and Chen 1993). It corresponds to the set of mesoscale perturbations derived from the model output. In contrast, turbulent kinetic energy occurred in association with wavelengths less than 10 km. This energy corresponds with the large eddy perturbations. Note, the size of the scale separation between the mesoscale and large eddy scale depends upon patch length.

Based upon the prior analysis, we adopt a wavelength of $3.0H$ to filter the output. The value of $3.0H$ obtained from our simulations differs from the range $1H$–$1.5H$ suggested by observations. This is because the model simulations used a relatively coarse resolution to resolve

[3] When clouds formed within the domain, we used the cloud top to obtain the wavenumber for $N_{\phi'-1}$.

TABLE 4b. Description of model experiments with moist processes turned off. The v component of the wind was set equal to 0.

Experiment	Patch sizes (L, km)	Special condition
Patch size and wind		
Exp. 1	64 (domain 1)	Background u wind 0.5 m s^{-1}
Exp. 2	32, 30, 26 (domain 2)	Background u wind 0.5 m s^{-1}
Exp. 3	7.5, 4, 16, 4, 8, 20 (domain 3)	Background u wind 0.5 m s^{-1}
Exp. 4	$0.25 < L < 1$ (domain 4)	Background u wind a constant, 0.5 m s^{-1}
Exp. 5	64	Observed (u) equals one-half background wind
Exp. 6	64	Observed (u) background wind
Exp. 7	64	Observed (u) equals twice background wind
Exp. 8	7.5, 4, 16, 4, 8, 20	Observed (u) equals one-half background wind
Exp. 9	7.5, 4, 16, 4, 8, 20	Observed (u) background wind
Exp. 10	7.5, 4, 16, 4, 8, 20	Observed (u) equals twice background wind
Soil moisture gradient		
Exp. 11	64	$\theta_{sl} = 0.177$ (dry patches), $\theta_{sl} = 0.257$ (wet patches)
Exp. 12	64	Sinusoidal distribution, $\theta_{sl_{min}} = 0.18$, $\theta_{sl_{max}} = 0.26$
Exp. 13	64	Jagged distribution for soil moisture
Stability and wind		
Exp. 14	64	Increased stability: original + $\delta\theta/\delta z = 3.5$ K km^{-1} $u = 0.5$ m s^{-1}
Exp. 15	64	Increased stability: original + $\delta\theta/\delta z = 7.0$ K km^{-1} $u = 0.5$ m s^{-1}
Exp. 16	64	Increased stability: original + $\delta\theta/\delta z = 3.5$ K km^{-1} Observed u wind
Exp. 17	64	Increased stability: original + $\delta\theta/\delta z = 7.0$ K km^{-1} Observed u wind
Specific humidity		
Exp. 18	64	Decreased $\tilde{q}$ to 50% of observed $u = 0.5$ m s^{-1}
Latitude		
Exp. 19	64	10° lat, $u = 0.5$ m s^{-1}
Exp. 20	64	50° lat, $u = 0.5$ m s^{-1}

the turbulent fields. As noted, the smallest eddies that the model could resolve in the horizontal direction with a minimum of four grid elements corresponded to a wavelength of 1000 m.

Figure 4 shows an example of filtered atmospheric fields obtained in experiment 6; that is, we show the mesoscale circulations that formed over these patches in the presence of a background wind. The mesoscale horizontal and vertical wind (u', w'), potential temperature (θ'), and specific humidity fields q' corresponded very well with observations of sea breezes and sea-breeze-like circulations produced with mesoscale models (e.g., Finkele et al. 1995; Lynn et al. 1995b).

Given the original fields and those like those shown in Fig. 4, we can obtain the vertical profiles of the triggering variables and their mesoscale and turbulent com-

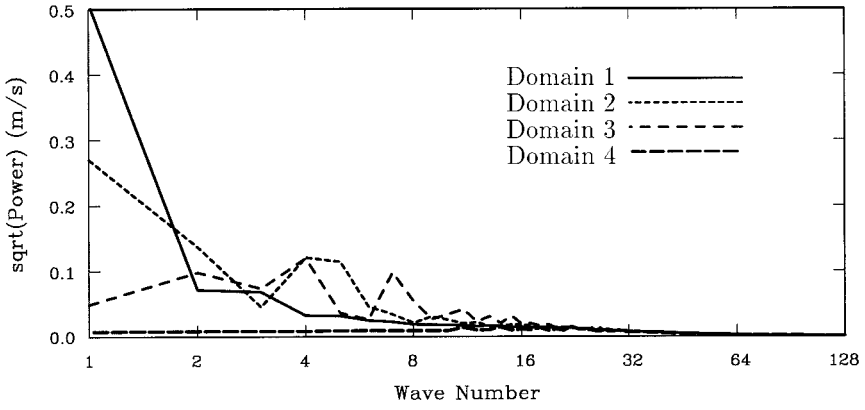

FIG. 3. Power spectrum analysis of the u component obtained in experiments using the domains shown in Fig. 2. Simulations were produced using the observed sounding, with a light background wind (0.5 m s^{-1}). The data were averaged over 12 h of simulation. Moist processes were turned off.

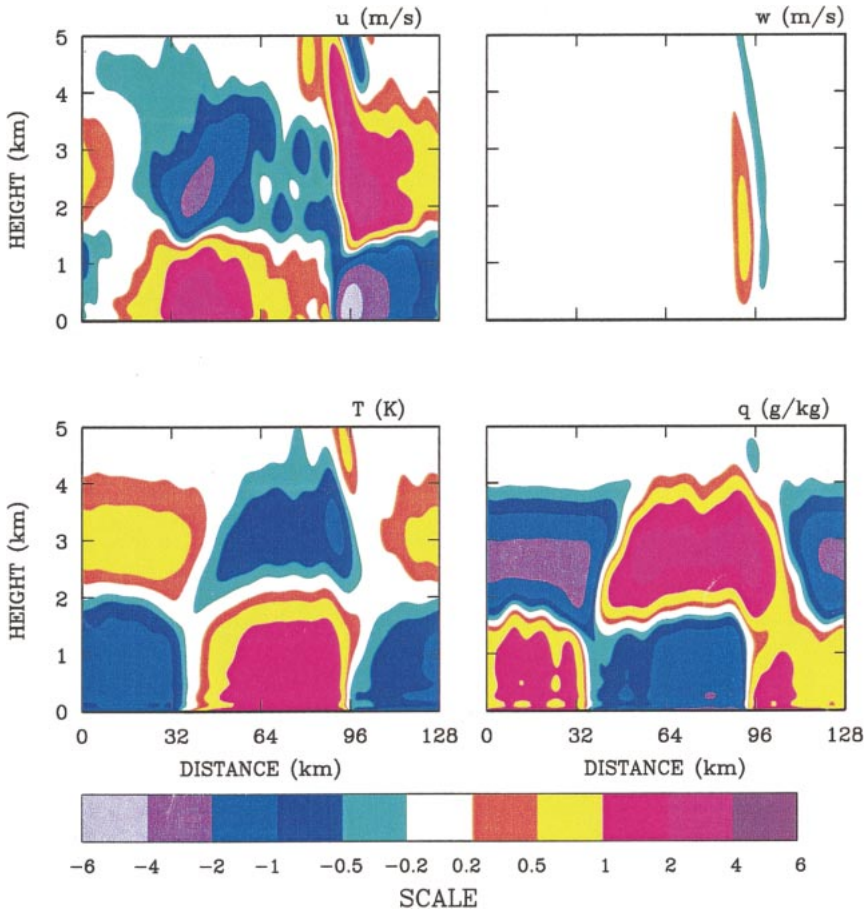

FIG. 4. Vertical west-to-east cross section of mesoscale perturbation fields obtained at 1300 LST in experiment 6. Note, the derived mesoscale perturbations were independent of *y*, or the north-to-south direction, since the data were averaged over the range of *y* values. The dry patch was located from 32 to 96 km.

ponents. We show examples of these profiles following the next section. Note,

$$\phi_o = \phi_o' + \phi_o'' + \phi_o''', \tag{12}$$

where the subscript zero indicates an average over the area of a parcel.

3. Results

a. The relationship between patch size and precipitation for various background winds

In general, the circulations simulated above the landscape heterogeneities shown in Fig. 2 moved inward toward the center of each dry patch. Mesoscale circulations occuring over individual dry patches produced rainfall over these patches. This rainfall occurred usually between 1000 and 1400 LST. Since the physics of the formation of rainfall over patches is well understood, no further details are given (e.g., Chen and Avissar 1994; Lynn et al. 1998).

We calculated the total accumulated rainfall from the simulations described in Table 4a by integrating over the whole domain in time and space. A linear interpolation gave the slope, *y* intercept, and regression coefficient. The relationship between the domain-averaged (accumulated) rainfall and average patch size was not monotonic (Table 5). Similar results occurred even when the regression analysis used the largest patch size within each domain, instead of the average patch size.

The reason that rainfall is not monotonic with average patch size can be explained by two examples, shown in Fig. 5a (experiment 1w) and Fig. 5c (experiment 4w). Simply, rainfall and its duration increase with increasing patch size,[4] but isolated rain clusters can occur even over small patches. Thus, domains (such as domain 3) with small patches can have more patches (and hence

[4] The forcing by the land surface depends upon the difference in heat flux between the wet and dry patches. Here, this difference at the time of rainfall formation was about 100 W m^{-2}, which can typically occur between different vegetation surfaces or in response to soil moisture differences (e.g., Sun and Mahrt 1994).

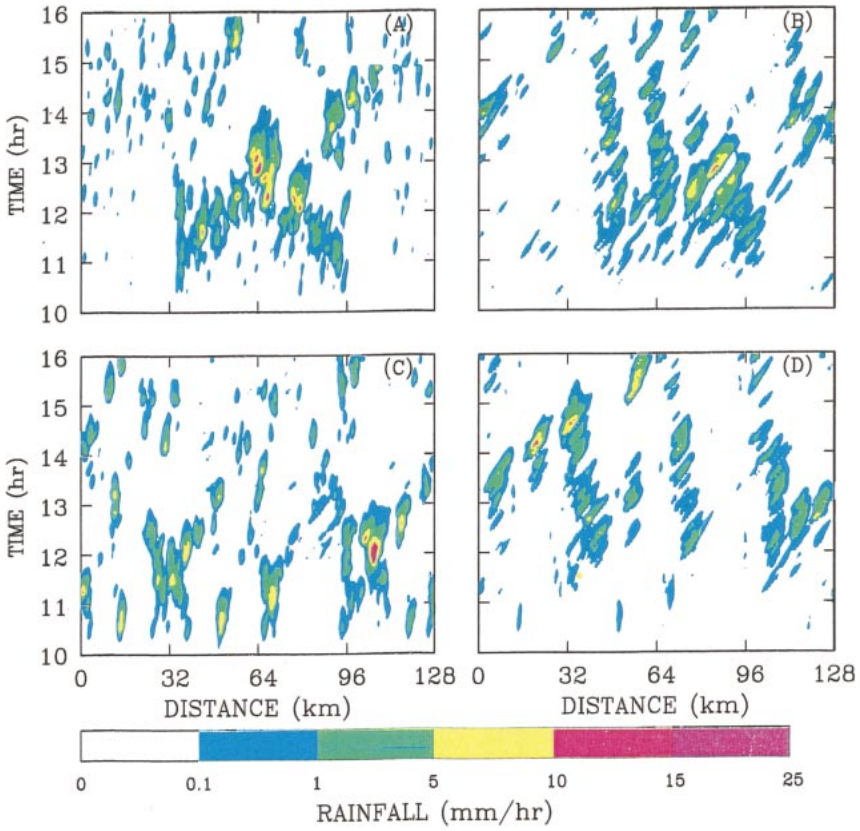

FIG. 5. Cross-sectional plots of rainfall vs time obtained in experiments (a) 1w, (b) 8w, (c) 4w, and (d) 11w.

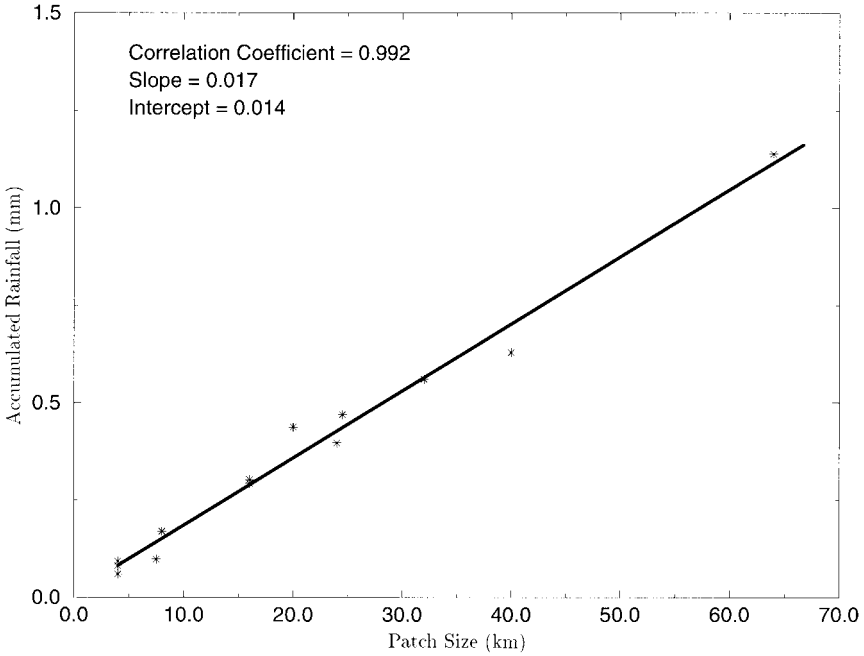

FIG. 6. Total accumulated rainfall vs patch size for the dry patches listed in Table 4, Experiments 1w–7w. Note, the rainfall was averaged over the length of each dry patch.

TABLE 5. Rainfall vs average patch size and largest patch size. Experiments 1w–7w were each produced using a light background wind. Experiments 8w–11w were produced using the observed (west-to-east) background wind. The correlation coefficient for average patch size vs rainfall for experiments 1w–7w was 0.32, while the correlation coefficient between the biggest patch size and rainfall was 0.45. For experiments 8w–11w, the correlation coefficient between the average patch size and rainfall was 0.77, while the correlation coefficient between the biggest patch size and rainfall was 0.79 (in these two sets, the range of the rainfall was relatively small).

Name	Average patch size (km)	Biggest patch size (km)	Accumulated rainfall (mm)
Exp. 1w	64	64	1.35
Exp. 2w	36	40	1.28
Exp. 3w	21.5	24.5	1.31
Exp. 4w	9	20	1.48
Exp. 5w	~4.5	~10	1.33
Exp. 6w	~3.0	~6	1.23
Exp. 7w	~0.5	~1.0	0.98
Exp. 8w	64	64	1.18
Exp. 9w	36	40	1.13
Exp. 10w	21.5	24.5	1.14
Exp. 11w	9	20	1.14

more rainfall ''clusters'') than domains with large patches (such as domain 1). In conclusion, the domain-accumulated rainfall is a function of both patch size and patch number.

Yet, it might not be obvious how to relate patch size and patch number to the triggering variables. To address this issue, we averaged the precipitation over individual patches and compared this averaged precipitation to patch size. The results show a simple, linear relationship between averaged precipitation over individual patches and the size of each patch (Fig. 6). In fact, the correlation coefficient was 0.99 for the simulations with $u = 0.5$ m s^{-1}.

The modeled relationship between rainfall and individual patch size can be explained by reference to linear theory. In the absence of a background wind, linear theory has been used to simulate the coarse features of mesoscale circulations. Dalu et al. (1991) have shown that the intensity of the flow increases proportionally with increasing patch size, for patches of size less than the local Rossby radius of deformation.

The results can also be explained in reference Fig. 7, which shows w_o', θ_o', and q_o' from experiments 1w and 4w. An analysis of Fig. 7 shows that the smaller patches, that is, 8- and 20-km, simulated triggering variables that were similar in magnitude to the 64-km patch. There is, however, some indication that the triggering variables over the 64-km patch had a longer timescale than over the other two smaller patches. This was most apparent when we looked at hourly averages of the vertical profiles (not shown). This likely explains why rainfall occurred over a longer period of time over the 64-km patch than over either the 20- or 8-km patch. Quite interestingly, w_o' and θ_o' spiked upward again over the smaller two patches, that is, at 1500 LST, as LGMCs redevelop over these patches.

Figures 5b and 5d show that the background (large-scale environmental) wind profile can affect the development of rainfall over patches. A background wind increases turbulent dissipation, which can reduce the generation of landscape-generated rainfall by mesoscale perturbations over small patches. On the other hand, a background wind blowing against the sea-breeze-like front on the downwind side of the dry patch can lead to an intensification of this front (this will be discussed in more detail later on). Figure 5b shows that the rainfall

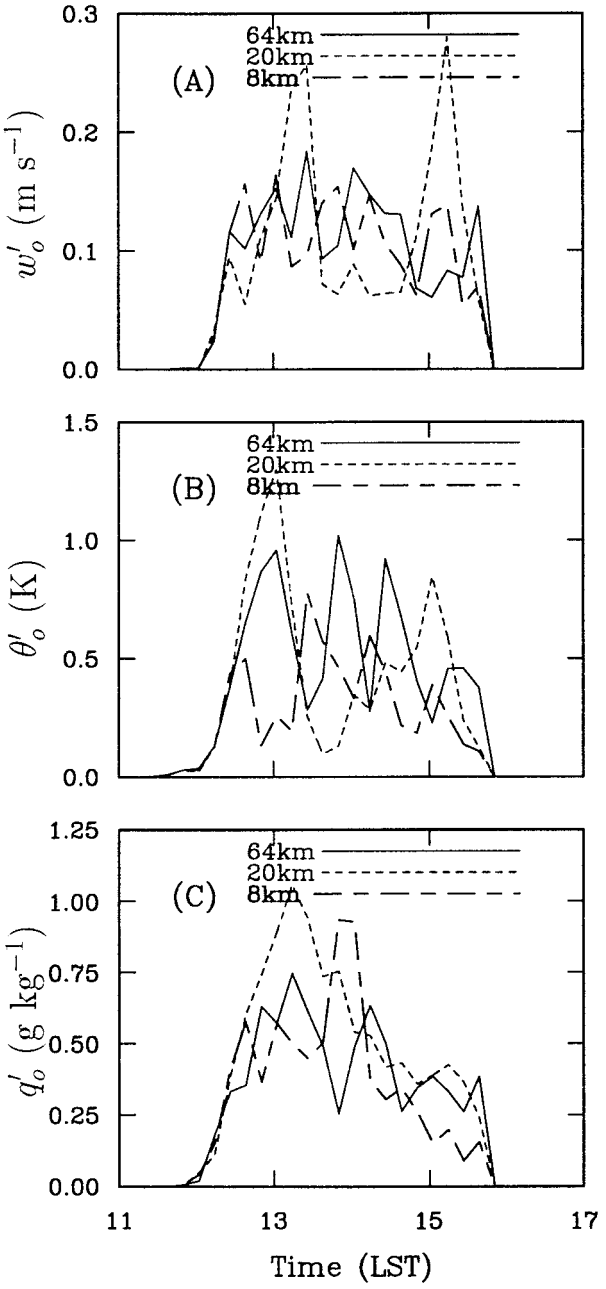

FIG. 7. The time variation of the set of mesoscale triggering variables obtained in experiments 1w and 4w, on the downwind side, for the patch sizes shown in the legend: (a) w_o', (b) θ_o', and (c) q_o'.

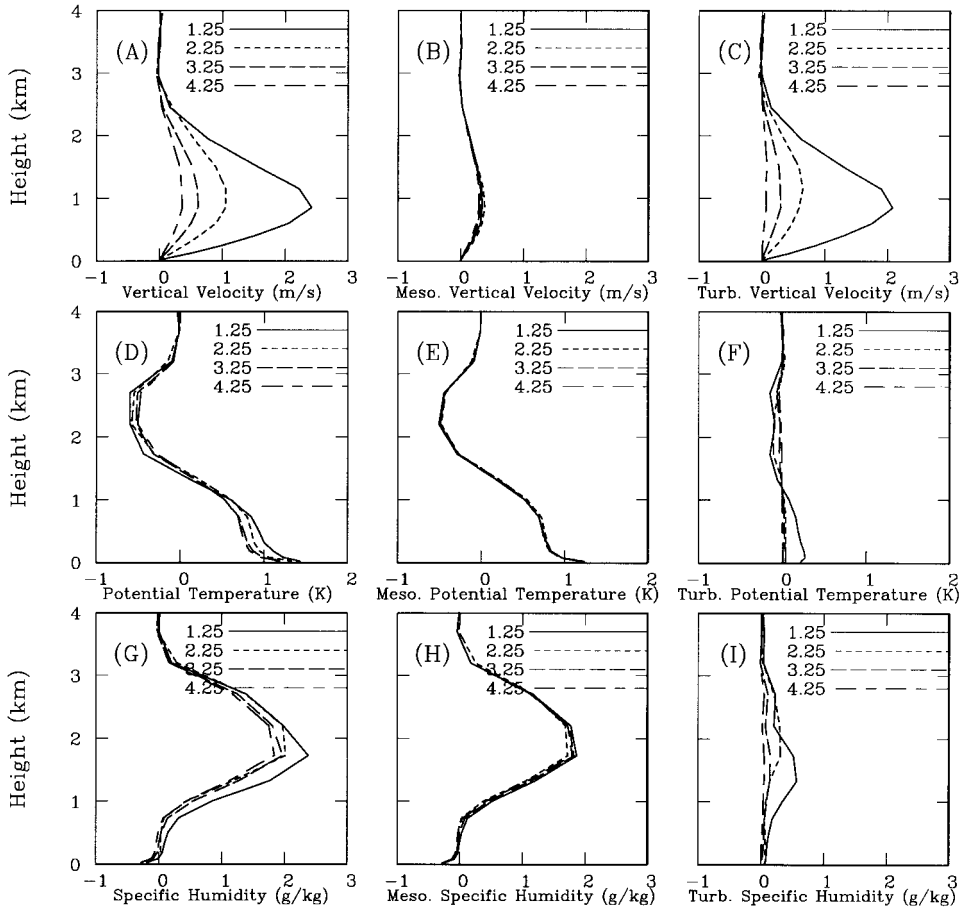

FIG. 8. Parcel vertical velocity, potential temperature, and specific humidity shown, respectively, in (a), (d), and (g). The graphs (b), (e), and (h) show the mesoscale contribution, ϕ', to each variable, while (c), (f), and (i) show the turbulent, large eddy scale contribution, ϕ''. The data was obtained from experiment 1 with parcels whose sides had the lengths shown in the legend (km). In the middle and bottom row, the data starts just above the origin (to prevent plotted data from cluttering the bottom of the plot).

was heavier on the downwind side of the dry patch in experiment 8w than on the upwind side, but Fig. 5d shows that experiment 11w produced less rainfall over the patches in domain 3 than experiment 4w. (The explanation follows in the next section.) Even with cyclic-periodic lateral boundary conditions used in this modeling study, the correlation coefficient for the set of experiments (experiments 8w–11w) was 0.95, indicating the importance of patch size.

The results suggest that trigger functions should be applied to multiple, individual patches, whose associated variables would depend upon patch size (and atmospheric background conditions). Moreover, the distribution over individual patches, such as in experiment 8w (domain 1), can be quite asymmetric. This suggests the need to represent a multiple of cloud populations within a domain and even over individual patches. The domain-averaged quantities could then be obtained from a cloud model as the integral over the domain of the regional- or global-scale atmospheric model of cloud-related variables occurring over individual patches.

b. Vertical profiles of triggering variables

Before proceeding, we thought it pertinent to examine the sensitivity of the triggering variables (and their components) to parcel size. As noted above, we assumed that the parcel size was 5.0625 km^2, or 2.25 km on a side. Figure 8 shows profiles of the triggering variables, including their mesoscale and turbulent components, for parcels with sides whose lengths are indicated in the figure. Experiment 1 was used to generate this figure.

The vertical velocity had a strong sensitivity to parcel size, but the other variables did not. Moreover, the sensitivity in the profiles of w_o, θ_o, and q_o to parcel size corresponded most closely to changes in the magnitude of w_o'', θ_o'', and q_o''. Thus, one who models these variables for a triggering function should take note of this sen-

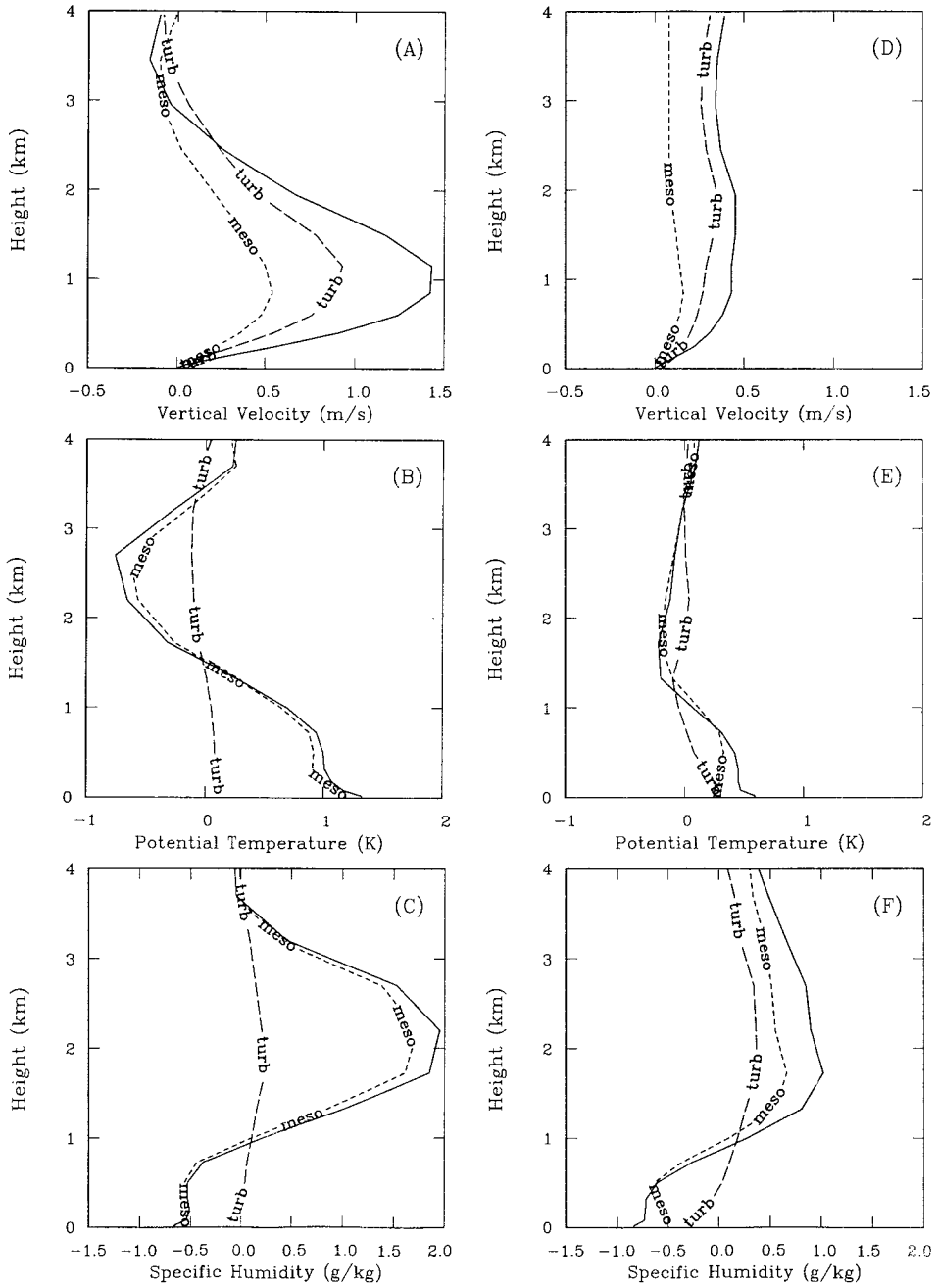

FIG. 9. Parcel vertical velocity, temperature, and moisture (solid line), and the mesoscale (labeled meso) and turbulent components of these variables (labeled turb). The experiment was experiment 6, and the triggering parcels were located on the downwind side of the dry patch. The data shown were averaged between 1000 and 1400 LST. Moist processes were turned off in experiment 6. The plots in (d), (e), and (f) show the same set of curves but for experiment 8w (with moist processes turned on).

sitivity. In contrast, the mesoscale variables, w'_o, θ'_o, and q'_o, did not show much sensitivity to parcel size. Thus, any parameterization developed for the mesoscale contribution to the triggering variables would not be sensitive to the size of the parcel, provided the parcel size was less than 4.25^2 km^2.

Figure 7 showed that rainfall related well to the growth of mesoscale perturbations in the triggering parcels, while Fig. 9 further demonstrates the need, as postulated by Rogers and Fritsch (1996) and Hong and Pan (1998), to incorporate mesoscale perturbations into triggering functions. For example, Figs. 9a–c show the ver-

tical profiles of ϕ_o, ϕ_o', and ϕ_o''[5] from experiment 6, where ϕ refers to the set of triggering variables for vertical velocity, potential temperature, and specific humidity. Note, we chose experiment 6 because this experiment used the observed wind, and would more likely be typical of cases occurring more frequently in situ. Both the variable w_o' and w_o'' need to be considered as important in the triggering of moist convection. The variable θ_o' had a much larger magnitude than θ_o'', while q_o' also had a much larger magnitude than q_o''. Each mesoscale perturbation should be included in a triggering function, while the turbulent perturbations can probably be ignored (for the parcel size considered here).

We can further test this hypothesis by examining the same set of perturbations, but for experiment 8w (moist processes turned on). Figures 9d–f show that the magnitude of the mesoscale and turbulent component of the triggering variables is sensitive to moist processes. The landscape-generated moist convection that occurred reduced the solar insolation at the land surface, which reduced the heating of the surface and the horizontal temperature gradient. Reduced surface heating limited the growth of bouyant, large eddy circulations. At the same time, though, latent heat release generated bouyancy in the upper PBL and cloud layer, while evaporative cooling caused by downdrafts strengthened and accelarated the movement of the sea-breeze-like fronts (Lynn et al. 1998). Thus, moist convection extended the vertical scale of the turbulent large eddies, while it reduced the magnitude and timescale of the developing mesoscale circulations. However, the mesocale contribution to the profile of the triggering variables still appears to be quite important, especially when considering the relative sizes of the mesoscale and turbulent perturbations.

A careful examination of model output (with moist processes turned off) suggests appropriate relationships for the mesoscale contribution to the triggering variables as a function of dimensionless height, $\hat{z}$:

$$w_o'(\hat{z}) = \begin{cases} w_o'(\max)(-0.0721 + 4.784\hat{z} - 6.524\hat{z}^2 + 2.061\hat{z}^3 - 0.076\hat{z}^4) & \hat{z} \le 1.5 \\ 0 & \hat{z} > 1.5 \end{cases} \quad (13)$$

$$\theta_o'(\hat{z}) = \begin{cases} \theta_o'(\max)(1.0 - \hat{z}) & \hat{z} < 1.25 \\ \theta_o'(\max)[-0.25 + (\hat{z} - 1.25)] & 1.25 < \hat{z} \le 1.50 \\ 0 & 1.50 < \hat{z} \end{cases} \quad (14)$$

$$q_o'(\hat{z}) = \begin{cases} q_o'(\max)(-0.50 + 1.50\hat{z}) & \hat{z} < 1.0 \\ q_o'(\max)[1.0 - 2.0(\hat{z} - 1.0)] & 1.0 < \hat{z} \le 1.5 \\ 0 & \hat{z} > 1.5. \end{cases} \quad (15)$$

To obtain the profiles for ϕ_o', one needs to find $\phi_o'(\max)$ and determine the relationship between it and variables such as patch size and background wind. Note, when moist processes occur, we found that one can approximate the shape of these curves as those given above. However, in Part II, Lynn et al. (2001) use budget equations for the purpose of more realistically determining the profile of the triggering variables when there are moist processes.

c. Sensitivity of triggering variables to background wind and patch size

Figure 10 shows that patch size had an important effect on the time variation of the variables $w_o'(\max)$, $\theta_o'(\max)$, and $q_o'(\max)$ (hereafter, we drop the word max when writing about these variables). For example, the maximum for each variable occurred first over the smallest of the patches (8 km), then over the middle-sized patch (20 km), and then over the largest of the patches (64 km). Note, the magnitude of the mesoscale triggering variables at any particular time was not always proportional to the size of the patches. But, the *e* folding time was smallest over the 8-km dry patch and largest over the 64-km dry patch.

We tested the sensitivity of the model results to (average) background wind (U) for the same patch sizes shown in Fig. 10. Because the magnitude of the mesoscale contribution to the triggering variables depended upon whether the parcel formed along the upwind or downwind side of the dry patch, we also show results from parcels on the upwind side of the 64-km patch. To simply the presentation of results, Fig. 11 shows the maximum obtained during the lifetime of each triggering parcel (after averaging over 30-min time periods). The results show that there exists a value of average

[5] The grid resolution of the model was too coarse to obtain small eddy perturbations; their impact on the atmosphere was represented through a turbulent kinetic energy closure scheme.

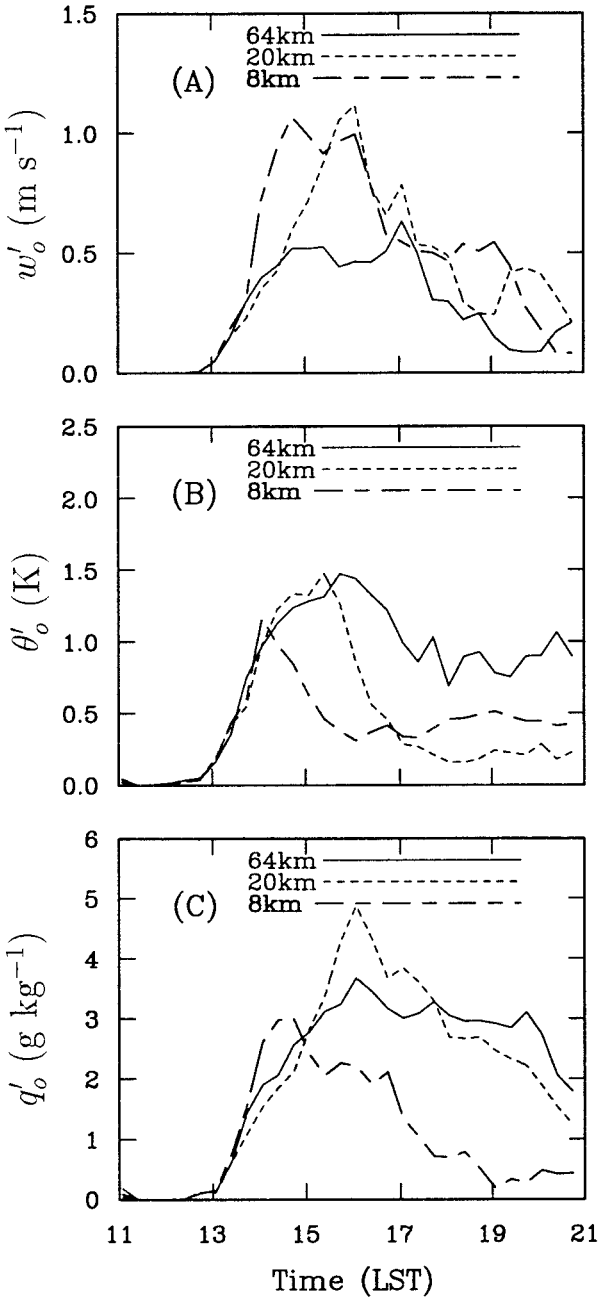

FIG. 10. Same as Fig. 7 but for the set of triggering variables obtained in experiments 1 and 3.

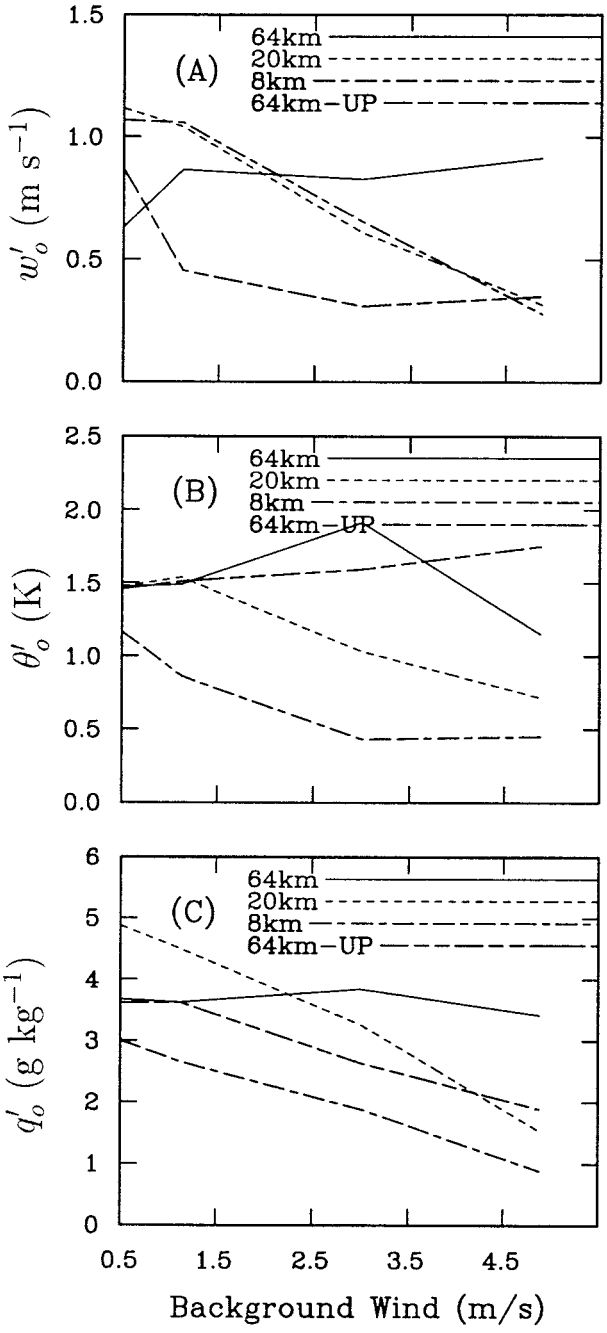

FIG. 11. The maximum value for the variables (a) w_o', (b) θ_o', and (c) q_o', obtained in experiments 1, 3, and 5–10, for the wind speeds shown. The symbol UP means that the triggering variables were obtained on the upwind side of the dry patch. Otherwise, the mesoscale triggering variables were obtained on the downwind side of the dry patch.

wind speed, U_o, at which the mesoscale triggering variables are a maximum.

In addition, Fig. 11 shows that U_o increases with increasing patch size. It also shows that upwind parcels generally produce weaker mesoscale vertical velocity and specific humidity than their downwind counterparts, especially as wind speed increases. However, they produce warmer mesoscale temperature perturbations, since the parcel is traveling over the warmest part of the dry patch. The results suggest that it would be useful to distinguish between triggering parcels between the upwind and downwind sides of a patch.

Differences in the development and dissipation of mesoscale circulations that occur over these patches produced the diversity of the modeled results. Lynn et al.

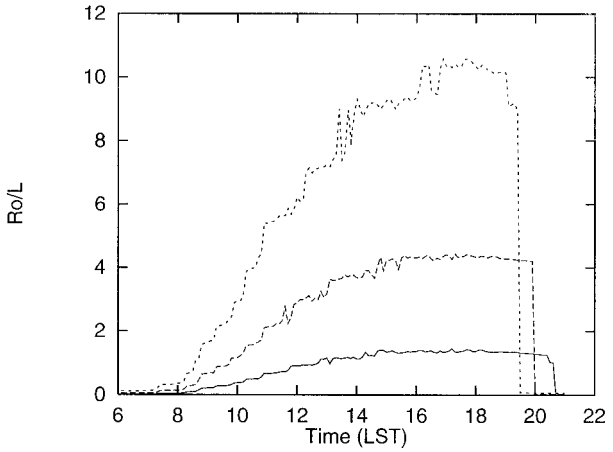

FIG. 12. The time variation of the ratio of local radius of deformation to patch length for the 64-km patch (experiment 1, solid line), the 20-km patch (experiment 3, dashed line), and 8-km patch (experiment 3, dotted line).

(1995b) used the Rossby radius of deformation to model such results. Lynn et al. (1998) suggested to use the local radius of deformation, R_o, which does not include Coriolis force as a variable. Both variables indicate the horizontal scale of the circulations likely to produce the strongest mesoscale circulations. The time dependence of the local radius of deformation divided by patch size (R_o/L) is shown in Fig. 12 for each of the patch sizes shown in Fig. 10. A strong relationship exists between the trigger variables and R_o/L. For example, the 8-km patch produced the largest rate of increase of R_o/L; the triggering variables over this patch reached their maxima before the other, larger patches. Thus, the dimensional number R_o/L can be used to model the dependence of the triggering variables on patch size.

The dependence of the triggering variables on background wind occurred because of the effect of background wind on perturbation temperature. Pielke (1984) and Bechtold et al. (1991) discussed the reasons why cases such as this produce the most robust vertical velocities. A synoptic wind blowing from a colder to a warmer surface weakens the horizontal (atmospheric) temperature gradient (here, on the upwind side of a dry patch of land), while a synoptic wind blowing from a warmer to a colder surface intensifies the temperature gradient (here, on the downwind side of the dry patch of land). Stronger temperature gradients lead to more robust mesoscale perturbations, while weaker temperature gradients lead to less robust mesoscale perturbations. The strongest vertical velocities occur when the circulation on the downwind side becomes stationary. Our results agreed with the previous modeling work of Pielke (1984) and Bechtold et al. (1991).

Note, our results suggest that the formulation by Rogers and Fritsch (1996) for w_i (our w_o') could be modified to better reflect the model results. For example, w_o' did not vary linearly with patch size, had different *e*-folding times over different patches, and fluctuated during the day. Moreover, w_o' has a peak around the middle of the atmospheric boundary layer, and not in the surface layer as suggested by Rogers and Fritsch (1996). Finally, w_o' had a strong sensitivity to background wind. We show later on that this variable also had a sensitivity to other environmental conditions such as atmospheric stability.

d. Impact of surface forcing, atmospheric stability, specific humidity, and latitude

Experiment 11 (domain 8), 12 (domain 9), and 13 (domain 10) examined the impact of soil moisture gradients upon the triggering variables. In experiment 11 (smaller gradient in soil moisture) and experiment 12 (a sinusoidal distribution in soil moisture), the mean sensible heat fluxes over the dry patch produced less sensible heat flux than in experiment 1 (the control), while the mean latent heat flux over the wet patch produced less than in experiment 1 (not shown). In experiments 11 and 12, the change in the triggering variables (not shown) was about 25% from the maxima obtained in experiment 1. This occurred because the forcing by the landscape patches changes linearly with the magnitude of the surface heat fluxes, as this determines the horizontal temperature gradients in the atmosphere. These results are consistent with those of Lynn et al. (1995a) and (1995b); they found a similar relationship for the mesoscale heat fluxes.

The effect of soil moisture gradients on the triggering variables was simply proportional to the change in the dimensionless variable $\Delta\overline{w'''\theta'''}^{d}/\langle w'''\theta'''\rangle$, where the first variable is the difference in heat flux between dry patch (superscript *d*) and the average heat flux (the last variable). Note, the triple prime indicates that these are parameterized heat fluxes. Figure 13a shows that this dimensionless variable reached a peak value at about 1000 LST in both experiments. Here, however, we are most concerned with changes in the magnitude of these curves for different distributions of soil moisture. This change was about 25%, which was similar to the change in the magnitude of the triggering variables.

In experiment 13 (jagged edges), the dimensionless variable $\Delta\overline{w'''\theta'''}^{d}/\langle w'''\theta'''\rangle$ (Fig. 13a) varied in time similarly to experiments 11 and 12. However, the time dependence of the triggering variables (not shown) resembled those of a patch size with intermediate size (e.g., 20 km $< L <$ 64 km), for a contrast in surface heat fluxes similar to experiment 1. A close examination of the model results suggested that the small patches (i.e., the jagged edges) surrounding the inner 32-km patch produced only very small perturbations. These results are in agreement with those of Avissar and Schmidt (1998), who showed that patches need to be about 5 km or larger to produce sizeable mesoscale perturbations in wind, temperature, and moisture. Therefore, a patch with jagged edges should be treated as a patch whose

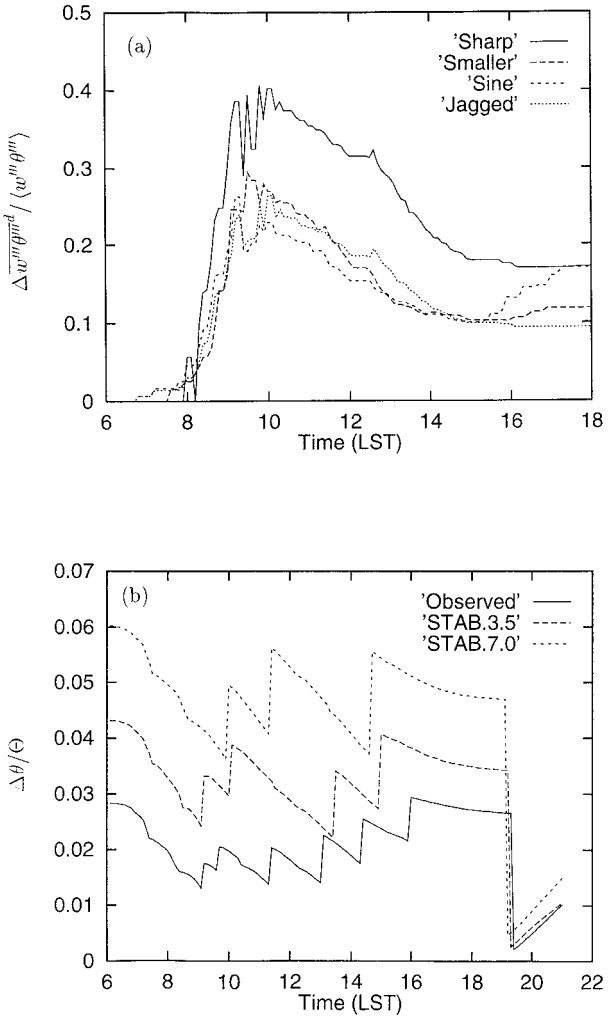

FIG. 13. The time variation of (a) $\Delta w'''\theta'''/\langle w'''\theta'''\rangle$ for experiments 1 (labeled sharp), 11 (labeled smaller), 12 (labeled sine), and 13 (labeled jagged). (b) The $\Delta\theta/\Theta$ for experiment 6 (the simulation with observed temperature profile and observed wind; labeled observed), experiment 16 (labeled STAB.3.5), and experiment 17 (labeled STAB.7.0). Table 4b explains the labels on the graphs.

dimensions cover the contiguous area of dry ground. (When this was done, the variable $\Delta\overline{w'''\theta'''}^{d}/\langle w'''\theta'''\rangle$ varied similarly in time for this inner patch to that obtained for the other dry patches.)

Segal et al. (1988) investigated the impact of abrupt versus progressive change of landscape types (or soil moistures) on mesoscale circulations. They found this effect to be relatively insignificant. Our results showed agreement with Segal et al. (1988), in that the mean heat fluxes from the dry and wet patches was much more important than the sharpness or irregularity of the gradient of soil moisture.

Four experiments, experiments 14–17, used either a light wind or the observed wind, with two profiles of temperature more stable[6] than the original sounding. The new soundings were typical of a summertime day with strong subsidence occurring within a strong high pressure system. This influenced both the surface fluxes and atmospheric turbulent fluxes, reducing the depth of the vertical mixing when compared to experiment 1.

The decrease in vertical depth of the developing mesoscale circulations had a negative impact on both w_o' and q_o' (not shown). Still, w_o' obtained with the observed background wind was larger than with the light wind, owing, in part, to the effect of background wind on the horizontal temperature gradients. The circulations in the simulations with the observed wind also converged earlier than with the light wind—when the heating was stronger and producing the largest mesoscale kinetic energy (Avissar and Chen 1993). However, the variable θ_o' remained nearly unchanged because mixing occurred over a more shallow PBL than with the observed sounding. Note, the turbulent large eddy vertical velocity, which depends strongly on the stability was even more greatly reduced than the mesoscale vertical velocity.

A dimensionless number that can be used to represent the impact of stability on the triggering variables is $\Delta\theta/\Theta$. This represents the difference in potential temperature between the free atmosphere (1000 m above the top of the PBL) and the average temperature within the PBL. Figure 13b shows that this variable increased with increasing atmospheric stability, varying by almost three times when comparing experiment 5 (the observed sounding) with experiment 15 (the largest static stability). The reader should keep in mind that this dimensionless variable is contained with the equation for the local radius of deformation. Here, the results suggested that the increase in stability led to a less optimal relationship between the local radius of deformation and patch size. This variable might be required only as a tuning variable to obtain more realistic results for the parameterization.

In experiment 18, the percentage change in q_o' (not shown) was proportional to the change in the initial profile of the domain average specific humidity, $\tilde{q}$ (hereafter, referred to as Q). This follows intuitively, since the potential size of the perturbations depends upon the initial profile of Q. However, the change in Q also led to a decrease in the sensible heat fluxes from both dry and wet patches. This had a negative impact on the development of the mesoscale circulations in experiment 18. Thus, the change in Q also affected the magnitude of the vertical profiles of w_o and θ_o; each was about 10% smaller than in experiment 1 (not shown).

The change in latitude had relatively little effect on the triggering variables (experiments 19 and 20). The

[6] A simulation with an atmospheric stability less than shown here produced results that did not add new information to the analsyis. This is because the stability was such that small perturbations grew very rapidly and deeply, over the first 3 h of the simulation.

patches were too small, and hence the mesoscale circulations too short lived, to allow for a significant impact of the Coriolis force on the triggering variables.

4. Summary and conclusions

A set of relatively high-resolution three-dimensional simulations were produced to investigate the triggering of moist convection over heterogeneous, west-to-east land surface domains. This moist convection was triggered by mesoscale circulations generated by the landscape heterogeneity. A set of triggering variables were identified. These variables depended strongly on the mesoscale contribution to the parcels's vertical velocity, temperature, and moisture. The size of the mesoscale perturbations depended upon the ratio of the local radius of deformation to patch size, the gradient of soil moisture between patches, as well as wind, stability, and specific humidity. Latitude had little affect on the mesoscale triggering variables. A monotonic (linear) relationship exists between the *local*-accumulated rainfall over *individual* patches and the size of these patches, but not the *domain*-accumulated rainfall and domain-averaged patch size. Thus, we suggest that cumulus parameterizations and their trigger functions for heterogeneous landscapes should be applied over multiple, individual patches within the domain, rather than to a single patch of average size. We suggested dimensionless numbers to be used in parameterizations for the parcel's triggering variables. Part II will discuss/show how to parameterize the triggering variables.

As noted, a linear relationship was obtained between rainfall and patch size. Perhaps, if we had obtained simulations where moist convection had occurred later in the simulation, the relationship found would have a more exponential shape (increasing nonlinearly upward with increasing patch size). This is because nonlinear advective affects become more important relative to linear processes as mesoscale circulations develop and move inward over the domain. Moreover, we would expect that the maximum rainfall would occur for patch sizes equal to the local radius of deformation (e.g., Lynn et al. 1998). The sizes of patches simulated here were all less than the midafternoon local radius of deformation.

The dataset used in this parameterization was obtained from a high-resolution model. We used a domain that could simulate the west-to-east structure of landscape-generated mesoscale circulations, with three-dimensional turbulence structure. In the future, we hope to be able to do fully three-dimensional simulations (e.g., using a symmetric domain). Finally, the development and dispensation of datasets such as the First ISLSCP Field Experiment (FIFE) and Large Scale Biosphere Atmosphere Experiment (LBA) can provide additional evaluation and refinement of the parameterizations suggested in this work.

Acknowledgments. The first author was supported by National Aeronautics and Space Administration Cooperative Agreement NCC 5-82. The second author is supported by the NASA Headquarters physical climate program, the NASA TRMM, and the interdisciplinary program of EOS. Each author thanks Drs. R. Adler and R. Kakar for their support, and two reviewers and Dr. D. Baker for their helpful and constructive suggestions. The views expressed herein are those of the authors and do not necessarily reflect the views of either agency.

REFERENCES

Avissar, R., and F. Chen, 1993: Development and analysis of prognostic equations for mesoscale kinetic energy and mesoscale (subgrid-scale) fluxes for large scale atmospheric models. *J. Atmos. Sci.,* **50,** 3751–3774.

——, and Y.-Q. Liu, 1996: Three-dimensional numerical study of shallow convective clouds and precipitation induced by land surface forcing. *J. Geophys. Res.,* **101,** 7499–7518.

——, and T. Schmidt, 1998: An evaluation of the scale at which ground-surface heat flux patchiness affects the convective boundary layer using large-eddy simulation. *J. Atmos. Sci.,* **55,** 2666–2689.

Balling, R. C., Jr., 1988: The climatic impact of a Sonoran vegetation discontinuity. *Climatic Change,* **13,** 99–109.

Bechtold, P., J. P. Pinty, and P. Mascart, 1991: A numerical investigation of the influence of a large-scale winds on sea-breeze- and inland-breeze-type circulations. *J. Appl. Meteor.,* **30,** 1268–1279.

Caughey, S. J., and S. G. Palmer, 1979: Some aspects of turbulence structure through the depth of the convective boundary layer. *Quart. J. Roy. Meteor. Soc.,* **105,** 811–827.

Chen, F., and R. Avissar, 1994: Impact of land-surface moisture variability on local shallow convective cumulus and precipitation in large-scale models. *J. Appl. Meteor.,* **33,** 1382–1401.

Cutrim, E., D. W. Martin, and R. Rabin, 1995: Enhancement of cumulus clouds over deforested lands in Amazonia. *Bull. Amer. Meteor. Soc.,* **76,** 1801–1805.

Dalu, G. A., R. A. Pielke, R. Avissar, G. Kallos, M. Baldi, and A. Guerrini, 1991: Linear impact of thermal inhomogeneities on mesoscale atmospheric flow with zero synoptic wind. *Ann. Geophys.,* **9,** 641–647.

Deardorff, J. W., 1975: The development of boundary-layer turbulence models for use in studying the severe storm environment. *Proc. SESAME Opening Meeting,* Boulder, CO, NOAA/ERL, 251–264.

Doran, J. C., and S. Zhong, 1995: Variations in mixed-layer depths arising from inhomogeneous surface conditions. *J. Climate,* **8,** 1965–1973.

Fankhauser, J. C., N. A. Crook, J. Tuttle, L. J. Miller, and C. G. Wade, 1995: Initiation of deep convection along boundary layer convergence lines in a semitropical environment. *Mon. Wea. Rev.,* **123,** 291–313.

Finkele, K., J. M. Hacker, H. Kraus, and R. A. D. Byron-Scott, 1995: A complete sea-breeze circulation cell derived from aircraft observations. *Bound.-Layer Meteor.,* **73,** 299–317.

Frank, W. M., 1983: The cumulus parameterization problem. *Mon. Wea. Rev.,* **111,** 1859–1870.

Hardy, K. R., and H. Ottersten, 1969: Radar investigations of convective patterns in the clear atmosphere. *J. Atmos. Sci.,* **26,** 666–672.

Hong, S.-Y., and H.-L. Pan, 1998: Convective trigger function for a mass-flux cumulus paratermization scheme. *Mon. Wea. Rev.,* **126,** 2599–2620.

Hong, X., M. J. Leach, and S. Raman, 1995: A sensitivity study of convective cloud formation by vegetation forcing with different atmospheric conditions. *J. Appl. Meteor.,* **34,** 2008–2028.

Houze, R. A., Jr., 1989: Observed structure of mesoscale convective systems and implications for large-scale heating. *Quart. J. Roy. Meteor. Soc.,* **115,** 425–461.

Kaimal, J. C., J. C. Wyngaard, D. A. Haugen, O. R. Coté, and Y. Izumi, 1976: Turbulence structure in the convective boundary layer. *J. Atmos. Sci.,* **33,** 2152–2169.

Kain, J. S., and J. M. Fritsch, 1992: The role of convective (trigger function) in numerical forecasts of mesoscale convective systems. *Meteor. Atmos. Phys.,* **49,** 93–106.

Klemp, J. B., and R. Wilhelmson, 1978: The simulation of three-dimensional convective storm dynamics. *J. Atmos. Sci.,* **35,** 1070–1096.

Konrad, T. G., 1970: The dynamics of the convective process in clear air as seen by radar. *J. Atmos. Sci.,* **27,** 1138–1147.

Lynn, B. H., and W.-K. Tao, 2001: A parameterzation for the triggering of landscape-generated moist convection. Part II: Zero-order and first-order closure. *J. Atmos. Sci.,* **58,** 593–607.

——, F. Abramopoulos, and R. Avissar, 1995a: Using similarity theory to parameterize mesoscale heat fluxes generated by subgrid-scale landscape discontinuities in GCMs. *J. Climate,* **8,** 932–951.

——, D. Rind, and R. Avissar, 1995b: The importance of mesoscale circulations generated by subgrid-scale landscape-heterogeneities in general circulation models. *J. Climate,* **8,** 191–205.

——, W.-K. Tao, and P. J. Wetzel, 1998: A study of landscape generated deep moist convection. *Mon. Wea. Rev.,* **126,** 928–942.

Mahrt, L., 1987: Grid average surface fluxes. *Mon. Wea. Rev.,* **115,** 1550–1560.

——, J. S. Sun, D. Vickers, J. I. MacPherson, J. R. Pederson, and R. L. Desjardins, 1994: Observations of fluxes and inland breezes over a heterogeneous surface. *J. Atmos. Sci.,* **51,** 2484–2499.

Nicholls, M. E., R. A. Pielke, and W. R. Cotton, 1991: A two-dimensional numerical investigation of the interaction between sea breezes and deep convection over the Florida pennisula. *Mon. Wea. Rev.,* **119,** 298–323.

Pielke, R. A., 1984: *Mesoscale Numerical Modelling.* Academic Press, 612 pp.

——, G. A. Dalu, J. S. Snook, T. J. Lee, and T. G. F. Kittel, 1991: Nonlinear influence of mesoscale land use on weather and climate. *J. Climate,* **4,** 1053–1069.

——, T. J. Lee, J. H. Copeland, J. L. Eastman, C. L. Ziegler, and C. A. Finley, 1997: Use of USGS-provided data to improve weather and climate simulations. *Ecol. Appl.,* **7,** 3–21.

Rogers, R. F., and J. M. Fritsch, 1996: A general framework for convective trigger functions. *Mon. Wea. Rev.,* **124,** 2438–2452.

Rutlege, S. A., and P. V. Hobbs, 1984: The mesoscale and microscale structure and organization of clouds and precipitation in mid latitude clouds. Part XII: A diagnostic modeling study of precipitation development in narrow cold frontal rainbands. *J. Atmos. Sci.,* **41,** 2949–2972.

Segal, M. W., R. Avissar, M. C. McCumber, and R. A. Pielke, 1988: Evaluation of vegetation effects on the generation and modification of mesoscale circulations. *J. Atmos. Sci.,* **45,** 2268–2292.

——, W. Schreiber, G. Kallos, R. A. Pielke, J. R. Garratt, J. Weaver, A. Rodi, and J. Wilson, 1989: The impact of crop areas in northeast Colorado on midsummer mesoscale thermal circlulations. *Mon. Wea. Rev.,* **117,** 809–825.

Sellers, P., and Coauthors, 1995: The Boreal Ecosystem–Atmosphere Study (BOREAS): An overview and early results from the 1994 field year. *Bull. Amer. Meteor. Soc.,* **76,** 1549–1577.

Smith, E. A., and Coauthors, 1992: Area-averaged surface fluxes and their time-space variability over the FIFE experimental domain. *J. Geophys. Res.,* **97,** 18 599–18 622.

Soong, S.-T., and Y. Ogura, 1980: Response of trade wind cumuli to large-scale processes. *J. Atmos. Sci.,* **37,** 2035–2050.

Stull, R. B., 1988: *An Introduction to Boundary Layer Meteorology.* Kluwer, 666 pp.

Sun, J., and L. Mahrt, 1994: Spatial distribution of surface fluxes estimated from remotely sensed data. *J. Appl. Meteor.,* **33,** 1341–1353.

Taconet, O., and A. Weill, 1983: Convective plumes in the atmospheric boundary layer as observed with an acoustic doppler radar. *Bound.-Layer Meteor.,* **25,** 143–158.

Tao, W. K., and J. Simpson, 1993: Goddard Cumulus Ensemble Model. Part I: Model description. *TAO,* **4,** 35–72.

Vidale, P. L., R. A. Pielke, L. T. Steyaert, and A. Barr, 1997: Case study modeling of turbulent and mesoscale fluxes over BOREAS region. *J. Geophy. Res.,* **102,** 29 167–29 188.

Walker, J. S., 1988: *Fourier Analysis.* Oxford University Press, 440 pp.

Wang, J., R. L. Bras, and A. B. Eltahir, 1996: A stochastic linear theory of mesoscale circulations induced by the thermal heterogeneity of the land surface. *J. Atmos. Sci.,* **53,** 3349–3366.

——, E. A. B. Eltahir, and R. L. Bras, 1998: Numerical simulation of nonlinear mesoscale circulations induced by the thermal heterogeneities of land surface. *J. Atmos. Sci.,* **55,** 447–464.

Wetzel, P. J., and A. Boone, 1995: A Parameterization for Land–Atmosphere–Cloud Exchange (PLACE): Documentation and testing of a detailed process model of the partly cloudy boundary layer over heterogeneous land. *J. Climate,* **8,** 1810–1837.

Young, G. S., 1987: Mixed layer spectra from aircraft measurements. *J. Atmos. Sci.,* **44,** 1251–1256.

——, 1988: Turbulence structure of the convective buondary layer. Part II: Phoenix 78 aircraft observations of thermals and their environment. *J. Atmos. Sci.,* **45,** 727–735.

Zawadzki, I. I., E. Torlaschi, and R. Sauvageau, 1981: The relationship between mesoscale thermodynamic variables and convective precipitation. *J. Atmos. Sci.,* **38,** 1535–1540.